

# Artifacts in regional gravity representations with spherical radial basis functions

## Research Article

K. Bentel<sup>1\*</sup>, M. Schmidt<sup>2</sup>, C. Rolstad Denby<sup>1</sup>

<sup>1</sup> Norwegian University of Life Sciences, Department of Mathematical Sciences and Technology, IMT, Postboks 5003, 1432 Ås, Norway

<sup>2</sup> Deutsches Geodätisches Forschungsinstitut, Munich, Germany

### Abstract:

With the increasing number of high-resolution gravity observations, which became available in the recent years, global Earth gravity models can be regionally refined. While global gravity models are usually represented in spherical harmonic basis functions with global support, a very promising option to model the regional refinements is the use of spherical radial basis functions with quasi-compact support. These functions are not necessarily orthogonal on a sphere, and usually, more functions are used in regional modelling than minimally needed from a global point of view. This makes the modelling more difficult. Furthermore, no techniques or choices of radial basis functions and other parameters in the regional modelling approach are established so far, as it is the case for global gravity modelling in spherical harmonics. In this article, a closed-loop simulation is used to investigate the mathematical modelling accuracy of different radial basis functions, which are compared to each other. Furthermore, artificial effects, which occur in the modelling results with very low levels of noise on the observations, are investigated. The whole study is performed on synthetic observations of a residual gravitational potential signal for the Himalaya area with different levels of noise. Spherical radial basis functions are a compromise between spatial and frequency localization, which are mutually exclusive. We show that spatial localization properties are even more important than frequency localization in the regional case, even though a band-limited signal is modeled.

### Keywords:

closed-loop simulation • radial basis function • regional gravity field modelling

© Versita sp. z o.o.

Received 16-05-2013 ; accepted 11-09-2013

### 1. Introduction

The Earth gravity field is most common given in global gravity models represented in spherical harmonic basis functions. Since spherical harmonics are global functions, the models are globally optimized best-fit solutions. That means, they do not necessarily represent small regional details in an optimal way. A very promising way to add regional details is the use of spherical radial basis functions. Regional gravity refinements can be observed by airborne gravity campaigns and by terrestrial gravimetry, while satellite gravity missions, like GRACE (Gravity Recovery And Climate Experiment, (Tapley et al. 2004)) or GOCE (Gravity Field and Steady-

State Ocean Circulation Explorer, (ESA 1999)), are used for signals from larger areas. Under the assumption that the longer wavelength part of the gravity field is represented in a global model in spherical harmonic basis functions, a residual gravity signal in a higher frequency bandwidth is modelled in spherical radial basis functions.

Spherical radial basis functions have been proposed and used by many others for Earth gravity modelling, for example (Schmidt et al. 2007, Eicker 2008, Freedon et al. 2009, Wittwer 2009, Panet et al. 2010) amongst many others. Foundations and mathematical details can be found in (Freedon et al. 1998, Freedon et al. 2004 or Wolf 2009). In a lot of applications, numerical integration is used to determine the regional gravity solutions. Here, parameter estimation techniques are used.

There are several advantages to parameter estimation, and the

\*E-mail: katrin.bentel@umb.no, Tel.: +47 6496 5456



most important ones are: the possibility to use irregularly distributed observation points (no grid interpolation is required), the possibility to straight forward combine different data types, the possibility to take errors into account, and the possibility of accuracy assessment of the results. Next to numerical integration and parameter estimation, (Kless et al. 2009, Antoni et al. 2009, and Fischer 2011) use non-linear algorithms to optimize the different parameters in regional gravity modelling simultaneously.

In a regional gravity representation in spherical radial basis functions, next to the basis functions themselves, a lot of parameters have to be chosen. These are the size of the area, margin widths, the number of radial basis functions, and a point grid for their location. The choice is not straight forward and not well-investigated so far. A closed-loop model is set up for this study in order to compare the performance of different radial basis functions, building up on the results in (Bentel et al. 2013). (Tenzer and Kless 2008) compare different spherical radial basis functions as well, however, we test a wider range of different types of functions. In Section 2 the closed-loop model is presented and explained. Section 3 shows results for different levels of white noise and the mathematic modelling accuracy with the different functions in question. Finally, in Section 4 artificial effects in the residuals are investigated.

## 2. Closed-loop simulations on regional gravity field modelling in spherical radial basis functions

A closed-loop simulation is set up in order to study the influence of the different parameters in the regional modelling approach. For all results shown in this paper, the same simulated regional gravitational potential observations are used. Thus, the results from the choice of different parameters in the regional modelling approach can be directly compared to each other. Even though it is not very realistic to consider gravitational potential values directly as observations, they are used here because the purpose of this work is to investigate the regional modeling process itself. Our findings also apply to scenarios where different gravity functionals are used. In the following, the closed-loop simulation is explained step by step.

**Step 1** First, synthetic residual gravitational potential observations are created. To obtain a residual signal, the difference between the geopotential models EGM2008, (Pavlis et al. 2012), and EGM96, (Lemoine et al. 1998), is used to simulate the removal of a reference gravitational potential model. Assuming that longer wavelength are modelled in a global representation in spherical harmonics, a bandwidth of spherical harmonic degrees 150 to 250 is used. This corresponds roughly to the sensitive bandwidth of the ESA gravity mission GOCE. The simulated observations are obtained via spherical harmonic synthesis and are only created in the Himalaya area, from  $75^{\circ}$  to  $90^{\circ}$  longitude and  $25^{\circ}$  to  $35^{\circ}$  latitude on a regular latitude-longitude grid with  $0.2^{\circ}$  spacing on a sphere with radius  $R = 6378.137$  km. Finally, observational errors are simulated in terms of added white noise. In Fig. 1 the simulated signal is given.

**Step 2** The simulated gravitational potential observations,  $\Delta V$ , together with simulated errors,  $e$ , are used to compute a regional gravitational potential field representation in spherical radial basis functions according to the linear model

$$\Delta V(\mathbf{x}) + e(\mathbf{x}) = \sum_{k=1}^K d_k B(\mathbf{x}, \mathbf{x}_k). \quad (1)$$

$B$  are the spherical radial basis functions, located on the sphere with radius  $R$  and depending only on the spherical distance between their location  $\mathbf{x}_k$  and the evaluation point  $\mathbf{x}$ . A point grid is needed to give the locations of the radial basis functions, which are the points  $\mathbf{x}_k$ , and the points  $\mathbf{x}$  are the observation points. To compute the regional gravity representation, the coefficients  $d_k$ , one for each radial basis function located at  $\mathbf{x}_k$ , have to be determined.  $K$  is the number of grid points in the area, which equals the number of radial basis functions.

**Step 3** The estimated coefficients  $d_k$  are used in a synthesis step to compute gravitational potential values on the sphere. This is performed on the sphere  $R$  on an independent latitude-longitude grid with  $0.25^{\circ}$  spacing to ensure a cross-validation of the results, instead of a reproduction of the observations. On the same  $0.25^{\circ}$  spacing grid, gravitational potential values are also synthesized from the original geopotential models. These are used as a reference to validate the modelling results.

**Step 4** The last step is the quality assessment of the representation in radial basis functions. The two synthesized fields are compared in each point, and the plots of their differences are evaluated. Another measure of the quality of the representation, which will be used throughout this paper, is an error root mean square percentage (RMS %) value. This value is derived by dividing the RMS of the errors (i.e. the differences between the two synthesized fields) by the RMS value of the signal. This relative error measure makes inter comparison between different modelling scenarios more clear.

A band-limited signal can be represented exactly in spherical radial basis functions if functions are chosen which exactly cover the signal's bandwidth and the representation is performed globally. Since the radial basis functions (see Eq. 2) have only quasi-local support and are strictly seen still global functions, omission errors are committed by restricting the modelling to a certain region. Additionally, the functions' spectral behaviour does not necessarily cover the signal bandwidth exactly. Spatial localization plays a much more important role in regional modelling than exact frequency coverage of the signal's bandwidth, as we will see in this study. There is a trade-off required between errors from leakage of the functions outside the area and errors from the signal spectrum which cannot be fully modelled. According to Heisenberg's

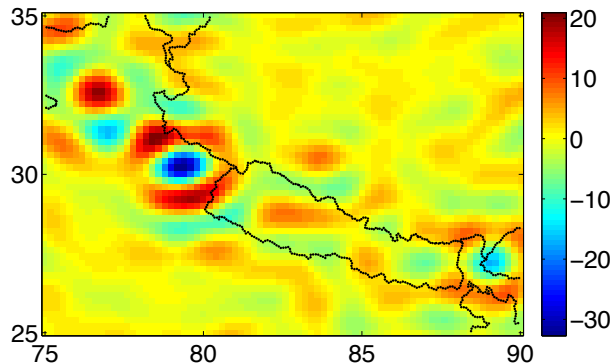


**Figure 1.** Regional residual gravitational potential signal [ $\text{m}^2/\text{s}^2$ ], spherical harmonic degrees 150 to 250, on the sphere in the Himalaya region obtained from the difference between the two geopotential models EGM2008 and EGM96.

uncertainty theorem only a compromise between spatial and frequency localization is possible. Therefore, the performance of different functions is evaluated, which all represent different compromises between spatial and frequency localization, that is, between spherical harmonics (which have perfect frequency localization but no spatial localization on the sphere) and the Dirac delta function (which has perfect spatial localization but no frequency localization); see (Freeden et al. 1998 or Freeden and Michel 2004). Tenzer and Kless (2008) compare four different spherical radial basis functions which all have an analytical expression and are non band-limited. These four functions lead to similar modeling results in their study. In contrast to their study, we locate all basis functions on a sphere with radius  $R$  and we also take into account band-limited functions, which play a role in gravity field modeling and can be directly derived from a global representation in spherical harmonics, see (Bentel et al. 2013). Since we don't require analytical expressions for the spherical radial basis functions under consideration, we can investigate several different types of band-limited functions next to a non band-limited function.

In our studies, we use three different sets of points in three different areas; these are points which are related to observations, points where the radial basis functions are located, and points where the synthesis is performed for evaluation of the modeling results. In a realistic case, the area where we perform the synthesis and evaluate the modeling results, would be the area of interest. In order to avoid boundary effects in the regional approach, the area of observations exceeds the area of synthesis by  $2^\circ$  and the area where radial basis functions are located exceeds the area of observations by another  $2^\circ$ . Previous numerical studies have shown that it results in smaller errors to choose the area of grid points for the locations of radial basis functions larger than the area of observations instead of the other way around. Other margin widths have been tested, but for the scenario in this simulation, the margin widths of  $2^\circ$  have shown to be a reasonable choice.

The determination of the unknown coefficients  $d_k$  is an ill-posed problem. On the one hand, more radial basis functions are used than minimally needed in a global scenario. Thus, no unique solution for the model parameters exists. On the other hand, the restriction of the representation to a certain area leads to ill-posedness, see for example (Schmidt et al. 2007). We use regularization to solve the ill-posed problem. To determine the regularization parameter  $\lambda$ , which gives the relative weighting between prior information and the observations, variance component estimation according to Koch and Kusche (2002) is used. Prior information is the expectation vector for the parameters, which is chosen to be zero because a residual signal is to be modelled, and its covariance matrix. The unity matrix is used, even though the parameters are not correlation-free. Test with the scalar product between the radial basis functions in the covariance matrix led to worse results in this simulation scenario than assuming them to be uncorrelated.

### 3. Different levels of white noise on the observations and different radial basis functions

The closed-loop simulation introduced in Section 2 is run for different radial basis functions and different levels of white noise added to the observations. All of the radial basis functions under consideration can be represented in Legendre polynomials  $P_n$  (see Schmidt et al. 2007) in the form of

$$B(\mathbf{x}, \mathbf{x}_k) = \sum_{n=0}^{\infty} \frac{2n+1}{4\pi} B_n P_n(\mathbf{r}^T \mathbf{r}_k), \quad (2)$$

thereby, the vectors  $\mathbf{r}$  and  $\mathbf{r}_k$  are unit vectors in directions of the points  $\mathbf{x}$  and  $\mathbf{x}_k$ , respectively, and the different functions are defined by the Legendre coefficients  $B_n$  according to Table 1. The Shannon, cubic polynomial, and Abel-Poisson functions can be found in Freeden et al. (1998) or Freeden and Michel (2004). The Blackman functions are defined in Schmidt et al. (2007) or Schmidt et al. (2006) and are derived from the Blackman window which is used in classical signal analysis. The Poisson multipole kernel is presented in Holschneider et al. (2003) or Chambodut et al. (2005). A Reuter grid, according to Freeden et al. (1998), is used to locate the radial basis functions. This grid gives quasi equidistantly distributed points on a sphere. The number of grid points, respectively their spacing, is derived from the maximum degree in the radial basis function and, thus, also from the width of the main lobe in the spatial domain. We determine the width of the main lobe from its width at half maximum, and it is simply derived from look up tables, since we use this value only to verify an appropriate grid spacing. A fixed Reuter control parameter  $\gamma$ , from  $\Delta\vartheta = \frac{\pi}{\gamma}$ , where  $\Delta\vartheta$  is the spacing of the grid points along the meridians, is chosen with  $\gamma = 450$  or  $\Delta\vartheta = 0.4^\circ$  for all different radial basis functions. This fixed point grid makes the results more comparable. All other parameters in the radial basis functions under consideration are chosen to fit to the grid spacing. This is the maximum frequency of the radial basis function, but also the width of the main lobe of the function in the spatial domain. Furthermore, the radial

Table 1. Definition of the radial basis functions under consideration

Shannon low-pass	$B_n = 1 \forall n \in [0, N], N = 250$
Shannon band-pass	$B_n = \begin{cases} 1 & \forall n \in [n_1, n_2] \\ 0 & \text{else} \end{cases}, n_1 = 150, n_2 = 250$
Blackman low-pass type I and type II	$B_n = \begin{cases} 1 & \text{for } n < n_1 \\ (A(n))^2 & \text{for } n = n_1, \dots, n_2 \\ 0 & \text{for } n > n_2 \end{cases}$ $A(n) = \frac{21}{50} - \frac{1}{2} \cos\left(\frac{2\pi(n-n_2)}{2(n_2-n_1)}\right) + \frac{2}{25} \cos\left(\frac{4\pi(n-n_2)}{2(n_2-n_1)}\right)$ type I: $n_1 = 250, n_2 = 450$ , type II: $n_1 = 200, n_2 = 400$
Blackman band pass (modified)	$B_n = \begin{cases} 0 & \text{for } n < n_1 - n_p \\ (A_{n_1}(n))^2 & \text{for } n \in [n_1 - n_p, n_1] \\ 1 & \text{for } n = n_1 + 1, \dots, n_2 - 1 \\ 1 - (A_{n_2}(n))^2 & \text{for } n \in [n_2, n_2 + n_p] \\ 0 & \text{for } n > n_2 + n_p \end{cases}$ $A_{n_1}(n) = \frac{21}{50} - \frac{1}{2} \cos\left(\frac{2\pi(n-(n_1-n_p))}{2n_p}\right) + \frac{2}{25} \cos\left(\frac{4\pi(n-(n_1-n_p))}{2n_p}\right)$ $A_{n_2}(n) = \frac{21}{50} - \frac{1}{2} \cos\left(\frac{2\pi(n-(n_2+n_p))}{2n_p}\right) + \frac{2}{25} \cos\left(\frac{4\pi(n-(n_2+n_p))}{2n_p}\right)$ $n_1 = 150, n_2 = 250, n_p = 110$
Cubic polynomial	$B_n = (1 - \frac{1}{n_{\max}} n)^2 (\frac{2}{n_{\max}} n + 1), n_{\max} = 450$
Poisson multipole	$B_n = (an)^l e^{-an}, l = 16, a = 32/400$
Abel-Poisson truncated	$B_n = h^n, h = \begin{cases} e^{-p} & \text{for } n \leq N \\ 0 & \text{for } n > N \end{cases}, p = 0.009, N = 450$
Abel-Poisson	$\sum_{n=0}^{\infty} \frac{2n+1}{4\pi} h^n P_n(r^T r_k) = \frac{1}{4\pi} \frac{1-h^2}{(1-2ht+h^2)^{3/2}}$ $B_n = h^n, h = e^{-p}, p = 0.009$

basis functions and the grid have to be chosen such that they are capable of modelling the highest signal frequencies which are to be represented. In the closed-loop model the grid point leads to a system with 3876 observations and 1437 unknowns. 1125 points are used in the cross-validation.

For the different radial basis functions, the regularization parameter  $\lambda$  derived from variance component estimation is very similar for each level of white noise. To make the results from the different functions for each level of white noise even more comparable to each other, a fixed regularization parameter  $\lambda$  is chosen for each noise level. The regularization parameters are given in Table 2 and are derived as mean values for each noise level from the individual parameters for each type of radial basis function from variance component estimation.

In Fig. 2 all the radial basis functions under consideration are plotted. The goal of this plot is not to show the detailed characteristics for each of the functions (since they might be hard to distinguish in this plot); these can be found in Bentel et al. (2013). But Fig. 2 shows that the main lobe in the spatial domain is about the same width for each of the functions, and there are great differences in the side-lobes and in the frequency behaviour of the functions.

Fig. 3 shows the error RMS percentage values from the closed-loop simulation (as explained in Section 2) for each radial basis function and level of white noise. For most radial basis functions, the error RMS percentage falls with the decreasing noise level, following the linear curve starting in the upper left corner of the plot. All the ra-

dial basis functions leave this linear curve at a certain noise level, and the error RMS value does not decrease anymore, even though the noise level decreases. The value, when the curve for the individual radial basis function leaves the linear curve, gives the level of the mathematical modelling accuracy with the respective radial basis function.

From the band-limited functions (band-pass and low-pass filters), the Shannon band-pass function has the least mathematical modelling accuracy in the regional representation, followed by the Shannon low-pass function. This can be explained by the strong oscillations in the spatial domain and especially outside the area of interest by the Shannon functions.

Three radial basis functions out of the nine under consideration have about the same model accuracy and give the best mathematical models under consideration. These are the Blackman low-pass function type I, the cubic polynomial function, and the Poisson multipole function, closely followed by the truncated Abel-Poisson function. Note that these radial basis functions have very different behaviours in the frequency domain, especially the Poisson multipole, which is a band-pass filter, while the others are low-pass filters. This shows, that for regional modelling the spatial behaviour plays an even more important role than the spectral behaviour.

To model a band-limited signal, the example of the only non band-limited radial basis function under consideration, the Abel-Poisson function, gives the worst results. The accuracy of the model with this radial basis function is even worse than the highest noise level

Table 2. Fixed regularization parameters  $\lambda$  (bottom line) for each level of white noise in  $\text{m}^2/\text{s}^2$  (top line)

noise	$10^{-1}$	$10^{-2}$	$10^{-3}$	$10^{-4}$	$10^{-5}$	$10^{-6}$	noise-free
$\lambda$	$2.4 \cdot 10^{-4}$	$3.2 \cdot 10^{-6}$	$4.3 \cdot 10^{-8}$	$1.1 \cdot 10^{-8}$	$1.1 \cdot 10^{-8}$	$1.1 \cdot 10^{-8}$	$1.1 \cdot 10^{-8}$

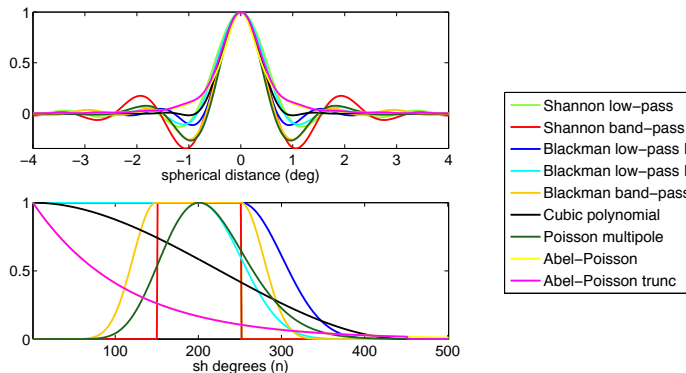


Figure 2. All radial basis function under consideration: spatial domain on top (scaled so that for each of them the maximum value is equal to 1), and the frequency domain at the bottom. See also Fig. 4 for more details on the functions of special interest.

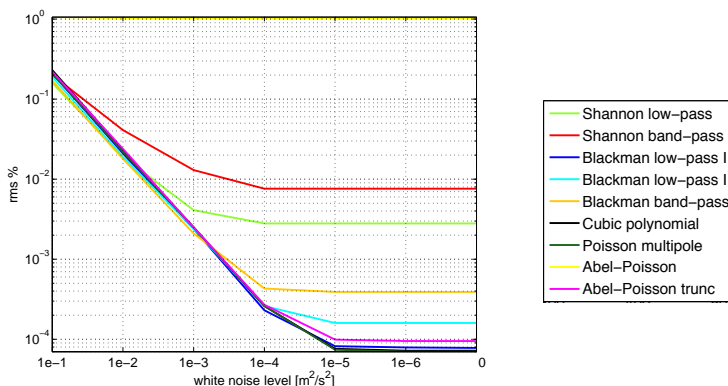


Figure 3. Results from simulations with different levels of white noise added to the observations and different radial basis functions: Relative root mean square values of the residuals for the different levels of white noise.

here, since the error RMS percentage values do not change with the noise level. This is due to the fact that in the model a fixed number of grid points for the locations of the radial basis functions are chosen and used for all of the radial basis functions. This number is too low for the non band-limited radial basis function. The number of grid points to locate the radial basis functions is derived from the maximum degree in the function. Thus, for the non band-limited radial basis function, an unlimited number of grid points would be optimal, what is of course not realizable numerically.

Out of all radial basis functions, three are studied in more detail. These are the Shannon low-pass function, the cubic polynomial function, and the truncated Abel-Poisson function. These three radial basis functions are plotted again in Fig. 4. Then, for these

three functions, the errors, i.e. the differences between the reconstructed signal from the representation in radial basis function and the expected signal, are plotted for each level of noise in Fig. 5. When comparing these plots to the results in Fig. 3 it can be seen that as long as the errors are dominated by white noise, the patterns in the residual plots seem random. But from the noise level where the errors are dominated by the mathematical modelling errors, there are oscillation-like effects to be seen. In repeated runs of the closed-loop model, the longitudinal stripes, which are very strong in the case of the Shannon function, and smaller and less clear for the other two functions from the white noise level of  $10^{-5} \text{ m}^2/\text{s}^2$  and below, are repeated as they can be seen in Fig. 5. However, the structures in the results which are dominated by noise, in

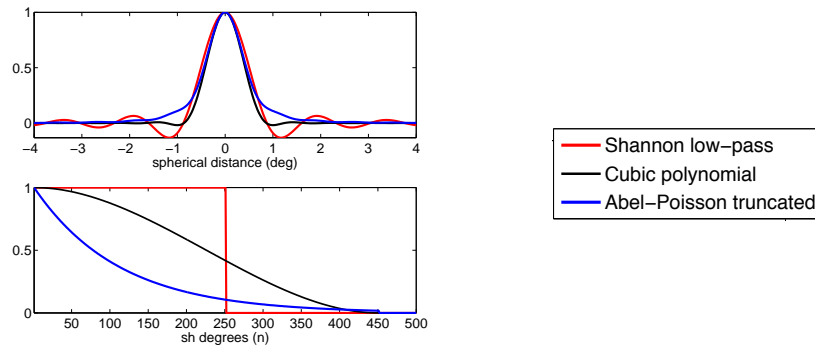


Figure 4. Radial basis functions which will be investigated in more detail: spatial domain on top, and the frequency domain at the bottom.

the first two rows and for the cubic polynomial and truncated Abel-Poisson function also in the third and fourth row in Fig. 5, will be different from different runs of the closed-loop model, in the way that the patch-like structures will have different shapes at different locations. A better understanding of the cause of the longitudinal structures will help to improve the accuracy of the mathematical model, what is our goal here. Thus, the results shall be investigated further in the following section.

#### 4. Different artificial effects in the residuals

In this section, the focus is on the artificial effects in the residuals which have been found in the previous section. Their possible causes are investigated.

##### 4.1. Effects due to the location of the radial basis functions

Different possibilities for point grids, which can be used to locate radial basis functions, and their effect on the regional modelling result are compared now. So far, in the simulations the Reuter grid has been used, but other possibilities for point grids are presented for example in Eicker (2008). Here, four other grids will be compared to the Reuter grid. Therefore, the same simulations as in the previous section are run again, but for different types of point grids and a white noise level of  $10^{-6} \text{ m}^2/\text{s}^2$ .

Five grids are tested and compared to each other here. These are, first, the Reuter grid as explained in Section 3. Second, another Reuter grid which is centered to the area of investigation instead of the zero meridian (as for the normal Reuter grid as we had used it before) and, thus, symmetric to the area of interest. Third is an icosahedron grid. Thereby, an icosahedron is subdivided until the desired number of points is reached. Then the points are projected onto the sphere. This grid is used by several others for regional gravity field modelling in radial basis functions, see Chambodut et al. (2005), Panet et al. (2005) or Eicker (2008). Fourth, a hexagonal grid, called here hexagonal grid I. Since this grid is very regular and the goal is to test if structures in the errors occur due to regularity, for the next example, the fifth, a hexagonal grid is used, where all

the center points of the hexagons are left out. This grid is called hexagonal grid II. Point distances are slightly decreased in comparison to the hexagonal grid I in order to obtain a very similar number of points in the area of interest from all the point grids.

Figures 6 to 8 show the different grids (along with the number of grid points, which equals the number of coefficients in the regional representation), the modelling results with the respective radial basis function and point grid, and the structure of the normal equation matrix. The same fixed value for the regularization parameter  $\lambda$  is used for all solutions, with  $\lambda = 1.1 \cdot 10^{-8}$ , as it has been determined in Section 3 for this noise level, in order to make the results as comparable as possible.

The results suggest that the point grid is not the reason for the artificial structures in the residuals with a low noise level. In all the three figures the error plots in the center column show very similar structures for the Reuter grids, the icosahedron grid, and the hexagonal grid I. In all the three cases, the errors with the hexagonal grid II are slightly higher, probably due to the irregularity of the grid points.

The structure of the normal equation matrices, in the right hand side column, looks the same for one and the same radial basis function for all the different point grids, but there are significant differences between the radial basis functions. The Shannon low-pass function has the largest side lobes and therefore the highest correlations between neighbouring points. This can be seen from the values different from zero next to the main diagonal. No correlations would lead to a diagonal matrix. When comparing the cubic polynomial and the truncated Abel-Poisson functions and their normal equations matrices it shows that there are more correlations with the Abel-Poisson function, even though this radial basis function has very smooth side-lobes and does not drop below zero in the spatial domain. The cubic polynomial function drops to small values closer to the main lobe in the spatial domain than the Abel-Poisson function (see Fig. 4). Therefore, the coefficients are less correlated for the cubic polynomial function. In the observation equation, which is obtained from Eq. (1), the grid points are organized latitude-wise. Thus, due to the margin of  $2^\circ$ , where the

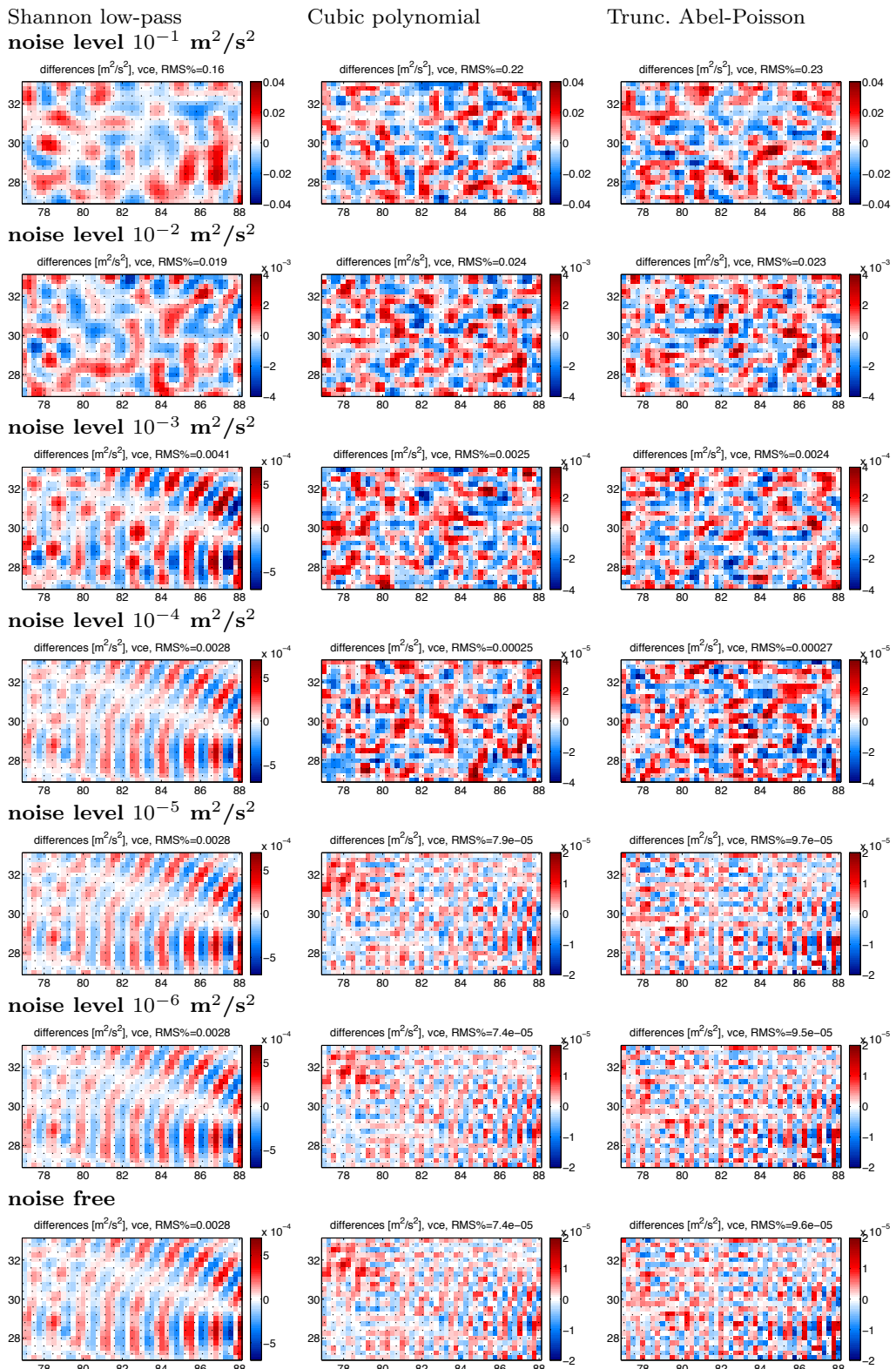
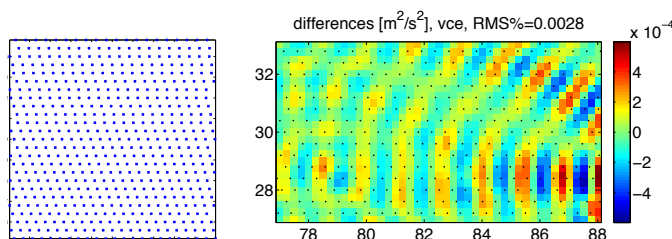


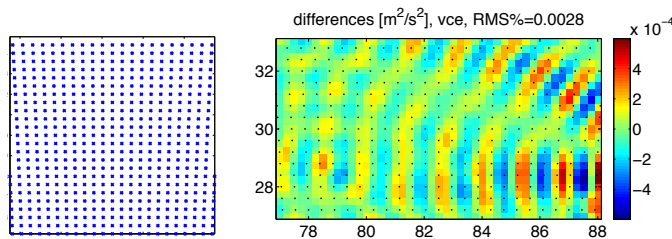
Figure 5. Residuals for the Shannon low-pass, the cubic polynomial, and the truncated Abel-Poisson functions for different levels of white noise on the observations. Note the individual range of the values in the plots! Since the error levels drop significantly when moving down the rows, individual colorbars have been chosen.

## Different point grids with the Shannon low-pass function

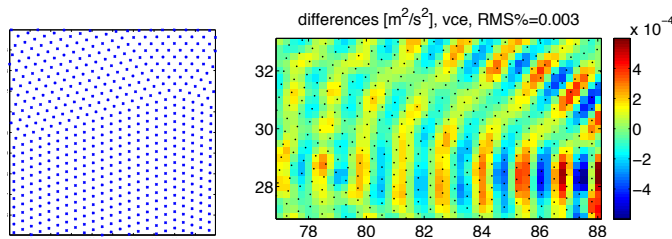
Reuter grid, 1437 coefficients



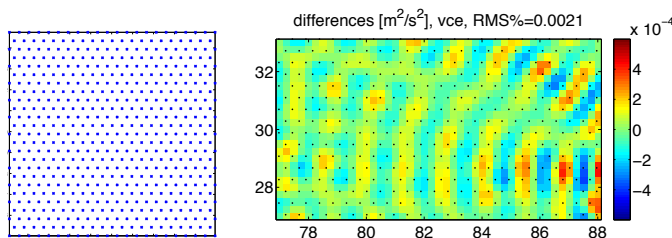
Reuter grid centered to the area, 1437 coefficients



Icosahedron grid, 1474 coefficients



Hexagonal grid I, 1411 coefficients



Hexagonal grid II, 1540 coefficients

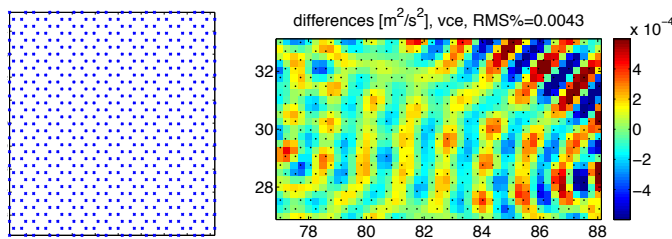
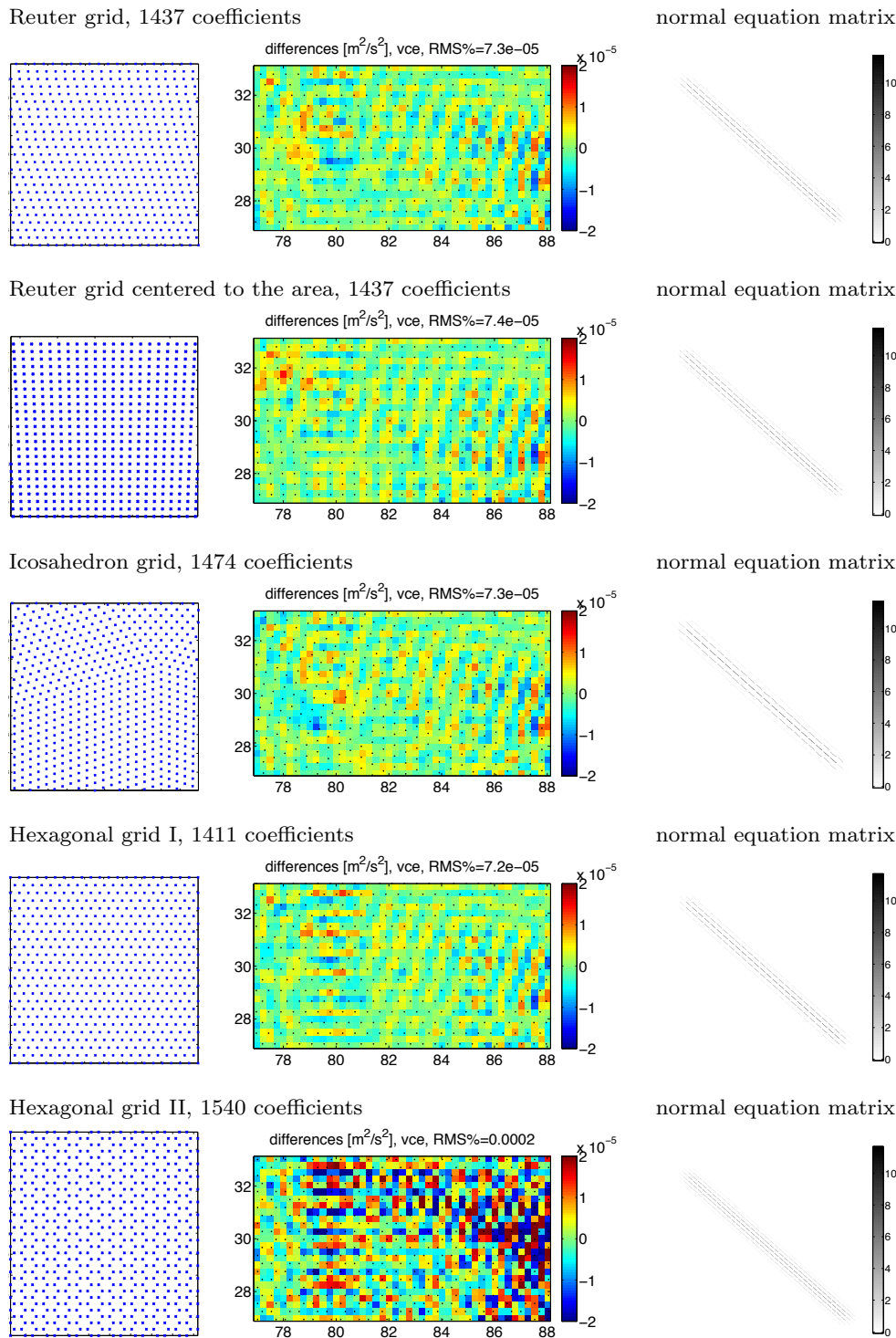


Figure 6. Simulations for different point grids. The column on the left hand side shows the different point grids, the center column shows the modelling errors in  $[\text{m}^2/\text{s}^2]$  for observations with noise in the order of  $10^{-6} \text{ m}^2/\text{s}^2$ , and the column on the right shows the normal equation matrix  $N$ . The same data is used as in the other simulations and all results are obtained with the Shannon low-pass function.

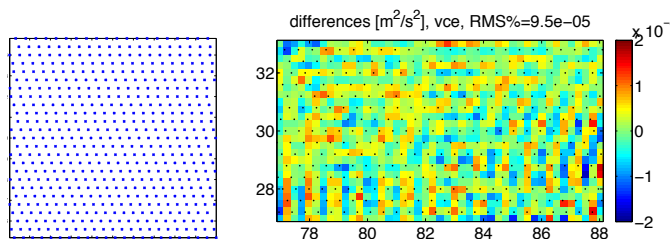
## Different point grids with the cubic polynomial function



**Figure 7.** Simulations for different point grids. The column on the left hand side shows the different point grids, the center column shows the modelling errors in  $\text{m}^2/\text{s}^2$  for observations with noise in the order of  $10^{-6} \text{ m}^2/\text{s}^2$ , and the column on the right shows the normal equation matrix  $N$ . The same data is used as in the other simulations and all results are obtained with the cubic polynomial function

## Different point grids with the truncated Abel-Poisson function

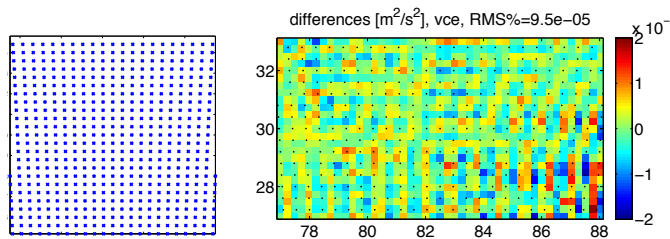
Reuter grid, 1437 coefficients



normal equation matrix



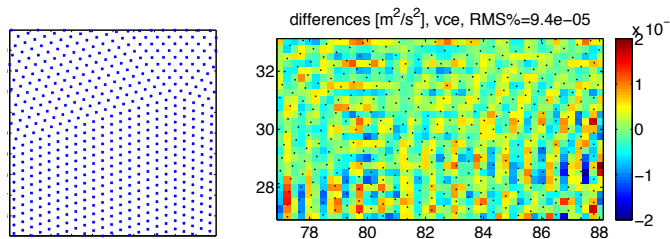
Reuter grid centered to the area, 1437 coefficients



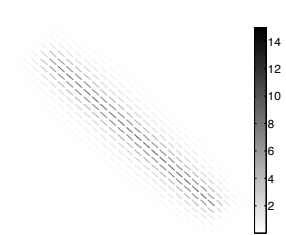
normal equation matrix



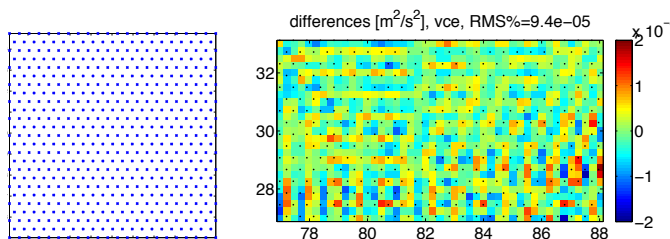
Icosahedron grid, 1474 coefficients



normal equation matrix



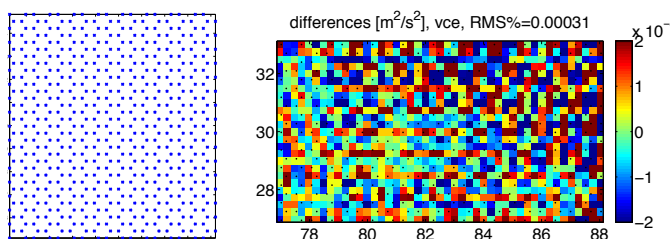
Hexagonal grid I, 1411 coefficients



normal equation matrix



Hexagonal grid II, 1540 coefficients



normal equation matrix



**Figure 8.** Simulations for different point grids. The column on the left hand side shows the different point grids, the center column shows the modelling errors in [m<sup>2</sup>/s<sup>2</sup>] for observations with noise in the order of 10<sup>-6</sup> m<sup>2</sup>/s<sup>2</sup>, and the column on the right shows the normal equation matrix N. The same data is used as in the other simulations and all results are obtained with the truncated Abel-Poisson function.

point grid exceeds the observations, there are zeros, respectively very small values, in the observation equation and therefore also zeros in the normal equations for the grid points on the margin. Table 3 shows the condition numbers of the observation equation matrices for the different radial basis functions and point grids computed with only the first two thirds of the singular values; see Naeimi (2013). There, the differences between radial basis functions are much more significant than the differences between grid points and one and the same radial basis function. Using the cubic polynomial or truncated Abel-Poisson function instead of the Shannon low-pass functions improves the condition number of the observation equation matrix by ten orders of magnitude, while the change in point grid has only smaller effects.

Concluding from all the findings with the different point grids in question and this closed-loop simulation, the actual type of point grid only plays a minor role. However, it is important to choose the appropriate number of grid points for the signal to be represented, and the points have to be distributed evenly across the area of interest. A point grid like the example of the hexagonal grid II is not recommended.

#### 4.2. Effects due to the regional signal

The oscillation-like effects, which occur in the results obtained from observations with a low noise level, see Fig. 5, could not be explained with the structure of the point grid in Section 4.1. Thus, possibly, these artificial structures occur due to effects related to the area of interest and the signal structure. Now different signal structures are tested and structures in the residuals investigated. In all the simulations here, a Reuter grid, centered to the area, is used, and white noise in the order of  $10^{-6} \text{ m}^2/\text{s}^2$  is added to the observations.

In the first test, the set of observations, which was used throughout all the previous examples, is flipped from left to right and used in the closed-loop simulation. The results from the closed-loop simulation with the mirrored signal are directly compared to the results with the original signal in Fig. 9. The original signal and errors from three different radial basis functions are shown in the left hand side column and the mirrored signal along with the results from the simulations with the same three functions on the right hand side. These results show clearly which effects are due to the observed signal, because only the artificial effects due to the input signal appear mirrored in the plots of the residuals, as all other parameters in the closed-loop simulation are exactly the same for the results in the left and in the right column of Fig. 9.

A comparison between the left and right columns shows mirrored structures in the residual plots from all the three radial basis functions. Not all structures are completely mirrored, but a good part of them, most evident in the residuals from the Shannon function, as the artificial structures are very distinct here. As expected, the root mean square values of the errors are about the same in the flipped cases and in the regular cases, as indicated above the plots.

The figures demonstrate that the mirrored part of the artifacts is due to area and signal effects. Since the area of interest is a rectangular area with sharp boundaries, this causes oscillations in the frequency domain, which appear in the reconstructed fields in the spatial domain when the estimated coefficients are used for synthesis. However, it is important to keep in mind that these effects are much smaller in magnitude than the errors in the residuals when noise-contaminated observations were used.

To investigate further where the artificial effects come from, the exactly same simulations as above (with noise in the order of  $10^{-6} \text{ m}^2/\text{s}^2$ ) are run for a constant and a linearly changing signal. Figure 10 shows the error plots from simulations with the three different radial basis functions, the centered Reuter grid, and the icosahedron grid. First for a constant signal and, second, for a linear signal. In the error plots in Fig. 10, artificial effects still appear for the Shannon low-pass and cubic polynomial functions. However, they are not, as in Fig. 9, originating from one corner of the area, but they are more or less parallel to the area boundaries, in both the case with a constant signal, and the case with a linear signal. This demonstrates clearly that these effects are due to the radial basis function's oscillations. The only case which does not show these effects but random error patterns is the case of the truncated Abel-Poisson function and the constant signal. The truncated Abel-Poisson function has much smaller side lobes than the other two functions. However, in the case of the linear signal there appear some oscillation-like effects in the results from the Abel-Poisson function as well, since the coefficients have to reflect the linearly increasing signal from left to right. Nevertheless, the performance of the Abel-Poisson function in the case of the constant signal and the numerical findings here confirm the theoretical reasoning for the use of the Abel-Poisson function, as for example in Freedon et al. (1998).

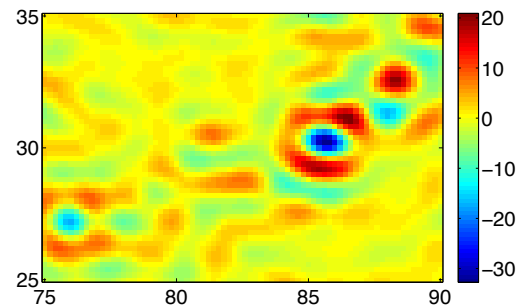
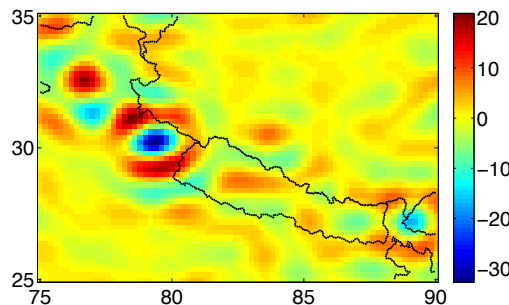
In addition to the results presented in detail here, enlarging the margins has been tested, in order to find out if the effects can be reduced. However, even for a  $5^\circ$  margin the error plots still show exactly the same structures. The same holds for additional tests with a smoothed signal boundary. In another additional test, the number of grid points was increased significantly to about one and a half times the number of grid points in the area. But even then the structure in the error plots still looked the same and were in the same order of magnitude.

#### 5. Summary and conclusions

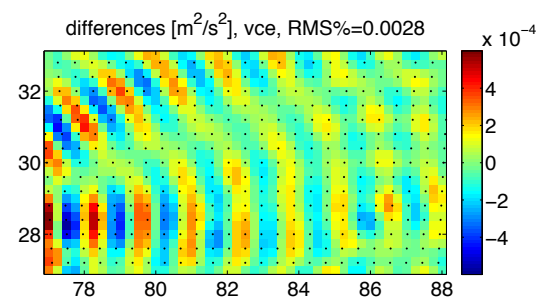
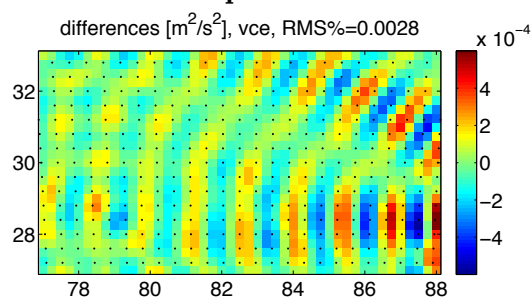
The closed-loop simulation for different radial basis functions and different levels of white noise has shown the mathematical modelling accuracy for different choices of radial basis functions. We have seen that the Blackman low-pass function type I, the cubic polynomial, and the Poisson multipole function lead to equally good modelling results, very closely followed by the truncated Abel-Poisson function. Note that these functions all have small side lobes besides the main lobe, and/or have only very small side lobes outside the area of interest.



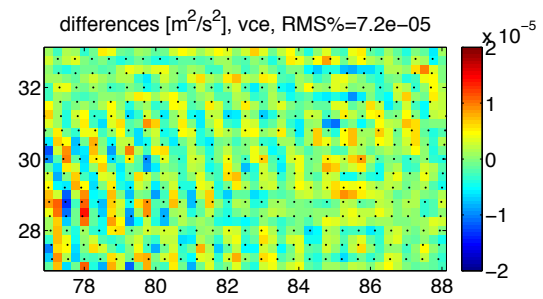
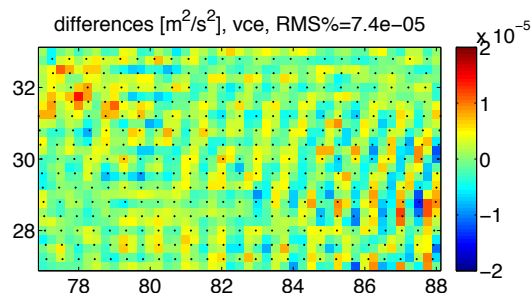
**Input signal + noise  $10^{-6} \text{ m}^2/\text{s}^2$**



**Shannon low-pass kernel**



**Cubic polynomial kernel**



**Truncated Abel-Poisson kernel**

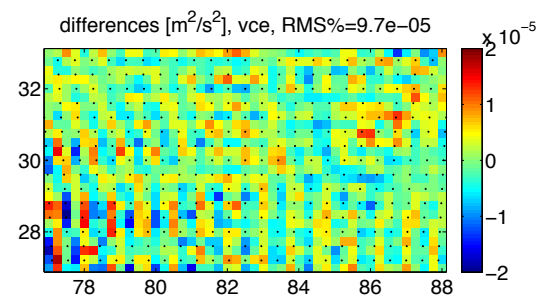
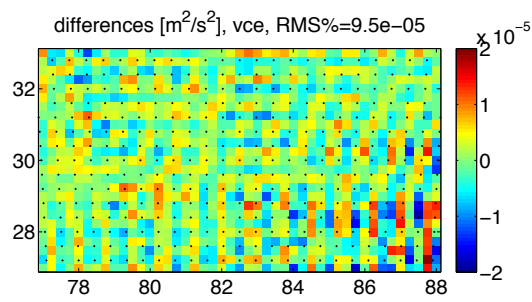


**Figure 9.** Gravity potential signal in  $[\text{m}^2/\text{s}^2]$  in the first row and errors in  $[\text{m}^2/\text{s}^2]$  of the simulation results obtained with regularization for the cubic polynomial, Poisson multipole, and truncated Abel-Poisson functions. In the right column the signal is flipped from left to right, all other parameters are exactly the same in both columns. To show the error structures as clearly as possible, each of the plots has its individual colorbar.

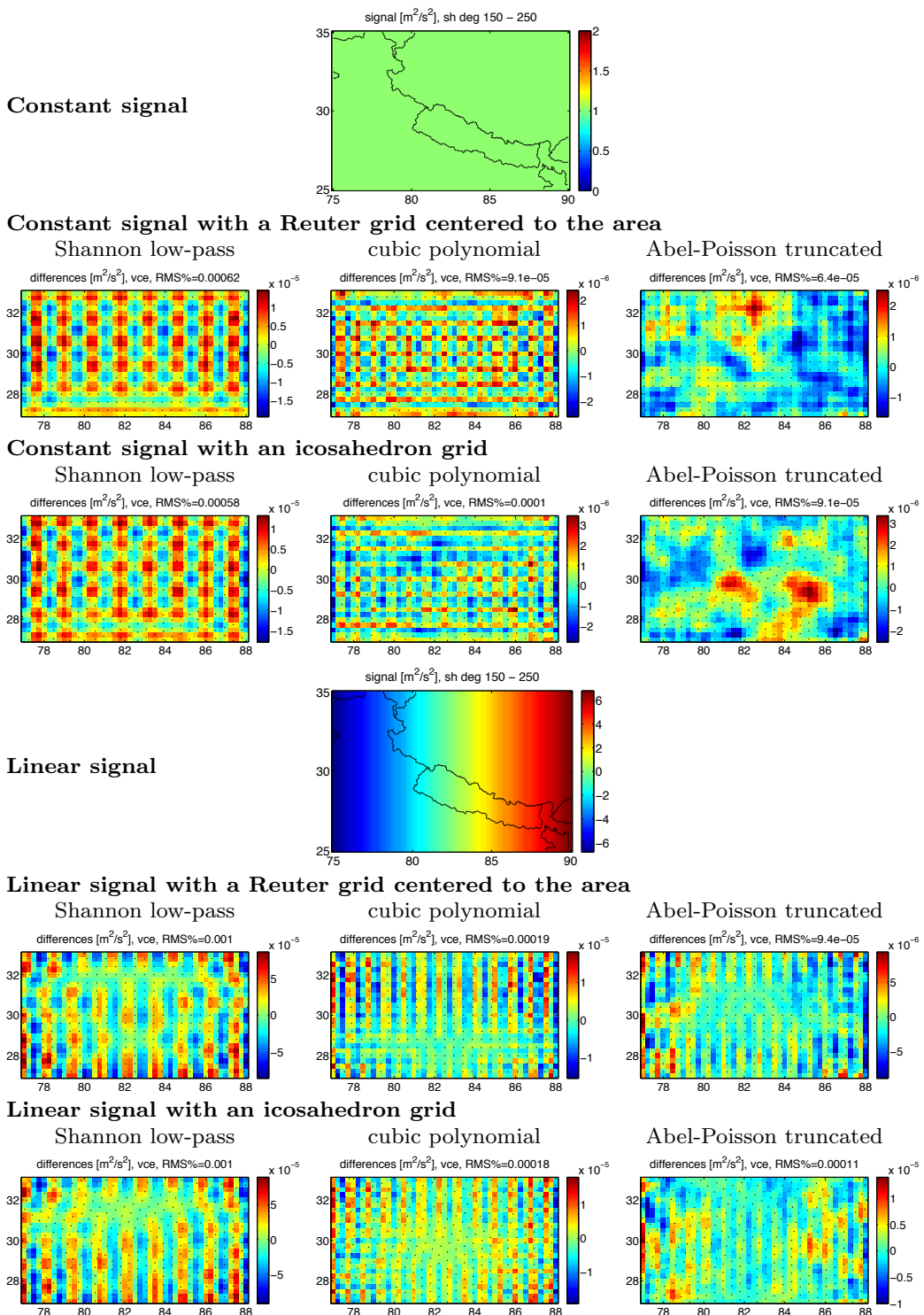


Figure 10. Test with constant and linear signal for the Shannon low-pass, cubic polynomial, and truncated Abel-Poisson functions and the centered Reuter and the icosahedron grids. Note that individual ranges for the colorbars in the plots of the residuals are chosen here in order to make the structures as visible as possible.

**Table 3.** Condition number (derived from the first two thirds of the singular values) of the observation equation matrix for the three different radial basis functions and the five different grids

	Shannon low-pass	Cubic polynomial	Truncated Abel-Poisson
Reuter grid	$3.3 \cdot 10^{12}$	$8.2 \cdot 10^2$	$3.5 \cdot 10^2$
Reuter grid centered	$3.3 \cdot 10^{12}$	$8.2 \cdot 10^2$	$3.7 \cdot 10^2$
Icosahedron grid	$3.3 \cdot 10^{12}$	$8.2 \cdot 10^2$	$3.7 \cdot 10^2$
Hexagonal grid I	$3.3 \cdot 10^{12}$	$8.3 \cdot 10^2$	$3.9 \cdot 10^2$
Hexagonal grid II	$3.5 \cdot 10^{12}$	$9.3 \cdot 10^2$	$4.4 \cdot 10^2$

In the frequency domain, these four functions show a very different behaviour. While the Poisson multipole is a band-pass filter, the other three are low-pass filters. This shows clearly, that in regional gravity modelling, the spatial behaviour of the functions plays a much more important role than the frequency behaviour. It is important to have good spatial localization. However, band-limited functions should be used to model a band-limited signal, as the poor results from the non-truncated Abel-Poisson function, which is an example for non band-limited radial basis functions, demonstrate.

Furthermore, reasons for artificial effects which occur in the simulations with low noise levels are investigated. It has been demonstrated that the effects are not due to the point grid, but solely due to the side lobes of the basis functions in the spatial domain. The truncated Abel-Poisson function has the smoothest behaviour in the spatial domain from the functions which are closely investigated. Therefore, this is the only function which does not show artificial effects in the residuals in the case of a constant signal. However, the function does not drop as fast with distance from the center as it does for example for the cubic polynomial function. Therefore, the individual functions are much more correlated, as it could be seen in the plots of the normal equation matrices.

The artificial effects are caused by the radial basis functions themselves, and can thus not be avoided. However, it is very important to keep in mind, that for the better performing radial basis functions, these errors are much smaller than errors due to noise on the signal.

Summing up all the findings, it is obvious that a compromise between spatial and frequency localization of the radial basis function has to be found. If the function is smooth enough in both domains, and has only very little oscillations in the spatial domain, the difference in the modelling results from these radial basis functions is only marginal. Furthermore, the differences in the modelling results for different point grids are very small, as long as the number of grid points is sufficient, and the points are equally distributed across the area of investigation.

The closed-loop simulation here is based on simulated gravity potential observations. However, radial basis functions are very well suited for gravity modelling from different types of observations, such as terrestrial, airborne, or satellite-based, as well as their combination. The findings here about numerical effects of the modelling procedure itself hold for the modelling from other types of

observations as well.

#### Acknowledgements

This study was made possible through funding by a "DAAD Doktorandenstipendium" from the German Academic Exchange Service.

#### References

- Tapley B.D., Bettadpur S., Watkins M., and Reigber Ch., 2004, The gravity recovery and climate experiment: Mission overview and early results. *Geophys. Res. Lett.*, 31(L09607).
- ESA, 1999, Gravity field and steady-state ocean circulation mission. Reports for mission selection: The four candidate Earth explorer core missions, ESA SP-1233(1).
- Schmidt M., Fengler M., Mayer-Gürr T., Eicker A., Kusche J., Sánchez L., and Han S-H., 2007, Regional gravity modeling in terms of spherical base functions. *J. Geod.*, 81(1):17–38.
- Eicker A., 2008 Gravity Field Refinement by Radial Basis Functions from In-situ Satellite Data. Dissertation, Institut für Geodäsie und Geoinformation, Universität Bonn.
- Freeden W., Fehlinger T., Klug M., Mathar D., and Wolf K., 2009, Classical globally reflected gravity field determination in modern locally oriented multiscale framework. *J. Geod.*, 83:1171–1191.
- Wittwer T., 2009, Regional gravity field modeling with radial basis functions. PhD thesis, NCG, Nederlandse Commissie voor Geodesie, Netherlands Geodetic Commission, Publications on Geodesy 72, ISBN 978 90 6132 315 0.
- Panet I., Kuroishi Y., and Holschneider M., 2010, Wavelet modelling of the gravity field by domain decomposition methods: an example over Japan. *Geophys. J. Int.*, 184(1):203–219.
- Freeden W., Gervens T., and Schreiner M., 1998, Construc-

tive Approximation on the Sphere With Applications to Geoscience. Oxford Science Publications, ISBN 019853682.

Freedon W. and Michel V., 2004, Multiscale Potential Theory With Applications to Geoscience. Springer Basel AG, ISBN 081764105X.

Wolf K., 2009, Multiscale Modeling of Classical Boundary Value Problems in Physical Geodesy by Locally Supported Wavelets. Dissertation, University of Kaiserslautern, Department of Mathematics, Verlag Dr. Hut, ISBN 978-3-86853-249-4.

Klees R., Tenzer R., Prutkin I., and Wittwer T., 2008, A data-driven approach to local gravity field modelling using spherical radial basis functions. *J. Geod.*, 82(8):457 – 471.

Antoni M., Keller W., and Weigelt M., 2009, Representation of regional gravity fields by radial base functions. In Michael G Sideris, editor, *Observing our Changing Earth*, volume 133 of International Association of Geodesy Symposia, pages 293–299. Springer, Berlin Heidelberg.

Fischer D., 2011, Sparse Regularization of a Joint Inversion of Gravitational Data and Normal Mode Anomalies. Dissertation, University of Siegen.

Bentel K., Schmidt M., and Gerlach Ch., 2013, Different radial basis functions and their applicability for regional gravity field representation on the sphere. *International Journal on Geomathematics*, 4:67–96.

Tenzer R. and Klees R., 2008, The choice of the spherical radial basis functions in local gravity field modeling. *Studia Geophysica et Geodaetica*, 52:287–304.

Pavlis N. K., Holmes S. A., Kenyon S. C., and Factor J. K., 2012, The development and evaluation of the Earth Gravitational Model 2008 (EGM2008). *Journal of Geophysical Research (Solid Earth)*, 117(B16):4406.

Lemoine F.G., Kenyon S.C., Factor J.K., Trimmer R.G., Pavlis N.K., Chinn D.S., Cox C.M., Klosko S.M., Luthcke S.B., Torrence M.H., Wang Y.M., Williamson R.G., Pavlis E.C., Rapp R.H., and Olson T.R., 1998, The development of the joint NASA GSFC and the National IMagery and Mapping Agency (NIMA) geopotential model EGM96. Technical report, NASA Technical Paper NASA/TP1998206861, Goddard Space Flight Center, Greenbelt, USA.

Koch K.-R. and Kusche J., 2002, Regularization of geopotential determination from satellite data by variance components. *J. Geod.*, 76:259–268.

Schmidt M., Han S-C., Kusche J., Sanchez L., and Shum C. K., 2006, Regional high-resolution spatiotemporal gravity modeling from GRACE data using spherical wavelets. *Geophys. Res. Lett.*, 33:1–4.

Holschneider M., Chambodut A., and Mandea M., 2003, From global to regional analysis of the magnetic field on the sphere using wavelet frames. *Physics of the Earth and Planetary Interiors*, 135(2-3):107–124.

Chambodut A., Panet I., Mandea M., Diament M., Holschneider M., and Jamet O., 2005 Wavelet frames: an alternative to spherical harmonic representation of potential fields. *Geophys. J. Int.*, 163(3):875–899.

Panet I., Jamet O., Diament M., and Chambodut A., 2005, Modelling the Earth's gravity field using wavelet frames. In Christopher Jekeli, Luisa Bastos, Joana Fernandes, and Fernando Sansò, editors, *Gravity, Geoid and Space Missions*, volume 129 of International Association of Geodesy Symposia, pages 48–53. Springer Berlin Heidelberg.

Naeimi M., 2013, Inversion of satellite gravity data using spherical radial base functions. Phd thesis, Institute of Geodesy, University of Hanover.